Nanoscale Advances

ROYAL SOCIETY OF CHEMISTRY

PAPER

View Article Online
View Journal | View Issue

Cite this: *Nanoscale Adv.*, 2023, **5**, 435

High-capacity polysulfide–polyiodide nonaqueous redox flow batteries with a ceramic membrane†

Mao Chen and Hongning Chen *

Nonaqueous redox flow batteries (NRFBs) have been regarded as promising large-scale electrochemical energy storage technology due to the wider solvent stable potential windows and greater selection of materials. However, the application of NRFBs is greatly limited considering the low capacity and high cost of active materials. In this work, we design and demonstrate a high-capacity polysulfide (PS)–polyiodide (PI) NRFB in Li-ion based 1,3-dioxolane (DOL) and 1,2-dimethoxyethane (DME) (v/v ~ 1 : 1) organic electrolyte. The high solubility and low cost of PS (5 M) and PI (4 M) can achieve the high capacity and high applicability of NRFBs, which is attractive for realizing large-scale stationary energy storage. The highest volumetric capacity of 28 Ah L^{-1} based on a full cell is achieved with 1.5 M PS-4 M PI. The high coulombic efficiency (~100%) and capacity retention (>99%) for 100 cycles in the PS–PI system is demonstrated by using a Li-ion conducting ceramic membrane. Voltage control is applied for both PS and PI to avoid the formation of irreversible solid Li_2S and I_2, which ensures the high stability of battery reaction. *In situ* UV-vis spectroscopy reveals the high reversibility of PS and PI in DOL/DME. A continuous flow mode test of the PS–PI system is also demonstrated to realize >300 hours stable cycling performance which implies good applicability for a long-term process. The successful demonstration of this high-capacity PS–PI nonaqueous system provides a new direction to promote the application of NRFBs in more fields.

Received 10th November 2022
Accepted 22nd November 2022

DOI: 10.1039/d2na00792d

rsc.li/nanoscale-advances

Introduction

Redox flow batteries (RFBs) are one of the most important electrochemical energy storage technologies for utilizing intermittent renewable energy (solar, wind *etc.*) due to its characteristics of decoupling power and energy.[1–6] Aqueous redox flow batteries (ARFBs) (*e.g.* vanadium redox flow batteries, VRFBs) have been widely used in large-scale stationary energy storage in recent years.[7–10] However, ARFBs have been suffering from serious water splitting and acid–alkali corrosion, which limits not only the cycling life but also the cell voltage.[11–14] In addition, the high-cost of metal-ion based raw active materials (*e.g.* V_2O_5) greatly decreases their competitiveness compared with commercial Li-ion batteries.[15–17] The current capital cost for VRFBs is about 450$ per kW h which is still far away for the target (<150$ per kW h) set by the US Department of Energy (DOE).[18–20] Low-cost and abundant organic active materials have been developed for ARFBs which broadens the range of catholytes and anolytes. For example, methyl viologen (MV)[21,22] and quinonoid molecules[23–25] have been applied in anolytes while ferrocyanide[26] and (2,2,6,6-tetramethylpiperidin-1-yl)oxyl (TEMPO)[18] have been applied in catholytes. However, the battery performance is still limited by the water stable potential window. Nowadays, nonaqueous redox flow batteries (NRFBs) have become more and more attractive considering the apparent advantages for promoting the application of RFBs.[27–29] Firstly, more active materials can be reversibly adopted in NRFBs due to the various types of nonaqueous solvents. For example, TEMPO in ethylene carbonate (EC) and diethyl carbonate (DEC) solvent,[30] and ferrocene ($FeCp_2$) and cobaltocene ($CoCp_2$) in *N*,*N*-dimethylformamide and 1,3-dioxolane (DOL) solvents[31] showed good reversibility and stability, which implies the diversity of NRFB solvents. Additionally, the organic solvent stable potential window is much wider than that of water so that the stability of NRFBs is supposed to be better than that of ARFBs. Several high-voltage NRFBs have been demonstrated such as 9-fluorenone (FL)/2,5-di-*tert*-butyl-1-methoxy-4-[2′-methoxyethoxy]benzene (DBMMB),[32] benzophenone (BP)/TEMPO,[33] $FeCp_2$/$CoCp_2$ (ref. 31) *etc.* However, most active materials used in NRFBs have very low solubility, which results in low capacity and low energy. For example, F. R. Brushett *et al.* demonstrated 2,5-di-*tert*-butyl-1,4-bis(2-methoxyethoxy)

Chemical Hybrid Energy Novel Laboratory, College of Chemistry and Environmental Engineering, Shenzhen University, Shenzhen, 518055, Guangdong, P. R. China. E-mail: hnchen@szu.edu.cn

† Electronic supplementary information (ESI) available: Photographs of PS and PI, EIS results of PS and PI at different stages, viscosity measurements of PS and PI, galvanostatic discharge–charge profiles of PS without LAGP, XRD results of LAGP, SEM images of a current collector, galvanostatic charge–discharge profiles of PI at various concentrations, galvanostatic charge–discharge profiles of PS at various concentrations, and schematic illustration and photograph of the flow cell configuration. See DOI: https://doi.org/10.1039/d2na00792d

benzene (DBBB) based NRFBs which can achieve a high voltage of 1.8 V but a low capacity of 5 Ah L^{-1} limited by the solubility of DBBB (0.4 M).[34] The advantages of NRFBs cannot be fully utilized due to the limitation of active material solubility. The development of high-solubility and low-cost active materials has become a key issue for NRFBs. One approach to increase the solubility of organic active materials is molecular modification, which is always accompanied by complex procedures.[15,35–37] Among all the candidates, the polysulfide–polyiodide (PS–PI) NRFB is very promising due to its high capacity, high stability and low cost. However, the PS–PI NRFB system still lacks comprehensive study considering the complicated reaction process of active materials. PS–PI ARFBs have been successfully demonstrated to achieve high volumetric capacity and coulombic efficiency.[38–40] Especially in 2021, Z. Li and Y. C. Lu designed a charge-reinforced ion-selective (CRIS) membrane for the PS–PI aqueous system to achieve a low capacity decay rate (0.005% per day and 0.0004% per cycle) over 2.9 months (1200 cycles) at 17.9 Ah L^{-1} volumetric capacity.[41] It should be noted that the stability is still extremely dependent on the pH of the aqueous electrolyte. Compared with the PS–PI aqueous system, the solubility of PS and PI in nonaqueous electrolyte is much higher, which is beneficial to achieve higher volumetric capacity.

In this work, a high-capacity PS–PI NRFB has been demonstrated with Li-ion based 1,3-dioxolane (DOL) and 1,2-dimethoxyethane (DME) (v/v ~ 1 : 1) organic electrolyte. The high solubility and low cost of PS (4 M) and PI (5 M) are attractive for achieving a large-scale high-energy NRFB system. Voltage control is applied for both PS and PI to avoid the formation of irreversible solid Li_2S and I_2, which can ensure the high stability of the battery reaction. *In situ* UV-vis spectroscopy for PS and PI revealed the high reversibility in DOL/DME. A volumetric capacity of 28 Ah L^{-1} based on a full cell has been achieved, which is one of the highest capacities reported in NRFBs. A Li-ion conducting ceramic membrane is applied in the PS–PI system to prevent the crossover between the catholyte and anolyte, which results in high coulombic efficiency (~100%) and capacity retention (>99%) after 100 cycles. A continuous flow mode test of the PS–PI system is also demonstrated to realize >300 hours stable cycling performance which implies good applicability for a long-term process. The successful demonstration of this high-capacity PS–PI nonaqueous system provides a new direction to promote the application of NRFBs in more fields.

Results and discussion

The working principle of a PS–PI NRFB is shown in Fig. 1a. The PS and PI dissolved in LiTFSI based DOL/DME solvent as the anolyte and catholyte are separated by a Li-ion conducting ceramic membrane which only permits the transportation of Li^+ to ensure the battery ionic charge equilibrium and prevents the crossover of active materials. The detailed synthesis process of the ceramic membrane was illustrated in our previous work.[42] The cell reactions of a PS–PI NRFB can be described as follows:

$$\text{Anolyte: } S_8^{2-} + 2e^- \rightarrow 2S_4^{2-}$$

$$\text{Catholyte: } 3I^- \rightarrow I_3^- + 2e^-$$

$$\text{Cell reaction: } S_8^{2-} + 3I^- \leftrightarrow 2S_4^{2-} + I_3^-$$

The solubilities of PS and PI has been measured to be 4 M (Li_2S_8) and 5 M (LiI) in DOL/DME, which are much higher than that of most active materials used in nonaqueous solvents. The color of PS and PI electrolyte increases from light to dark with the increase in the concentration as shown in Fig. S1.† The high solubility of the active material can further increase the volumetric capacity of the anolyte and catholyte. Viscosity is an important property of electrolytes which directly influences the pump power consumption and electrochemical performance of RFBs. The viscosity of PS and PI increases as the concentration increases but still remains in a reasonable range (<150 cP) as shown in Fig. S3,† which is much smaller than that of highly concentrated semi-solid suspensions.[43–45] Fig. 1b shows the CV results of 10 mM Li_2S_8 and 10 mM LiI in 1 M LiTFSI DOL/DME at scanning rates from 1–5 mV s^{-1}, which implies the good reversibility and stability of active materials used in this NRFB. The full cell voltage of the PS–PI NRFB is around 0.62 V, which can be compensated by the high-capacity in the aspect of energy

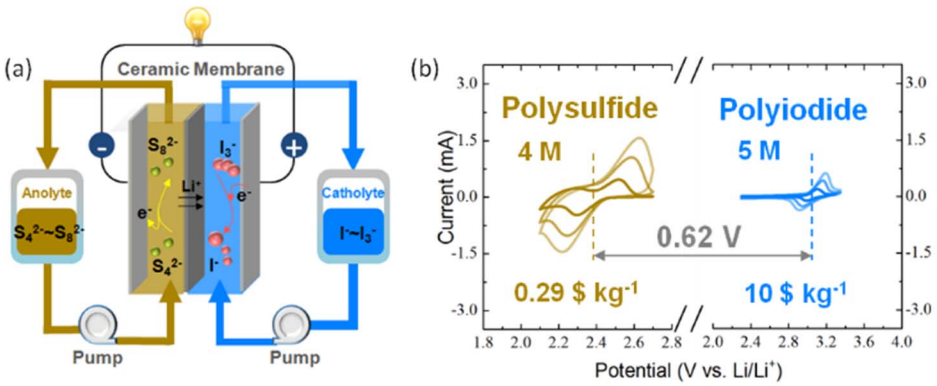

Fig. 1 (a) Schematic illustration of the polysulfide–polyiodide nonaqueous redox flow battery. (b) Cyclic voltammograms (CVs) of 10 mM Li_2S_8 and 10 mM LiI in 1 M LiTFSI DOL/DME (1 : 1 ~ v/v) at scanning rates from 1–5 mV s^{-1}.

density. In addition, the raw material costs of PS and PI are only 0.29$ per kg and 10$ per kg respectively,[38] which are much lower than that of V_2O_5 (24$ per kg) for commercial VRFBs.[19] The PS–PI NRFB can potentially realize a high-capacity and low-cost battery system for large-scale energy storage.

Voltage control is applied in the PS–PI NRFB to prevent the formation of irreversible and insoluble by-products considering the specific reaction pathway of PS and PI. Fig. 2a shows the CV results and reaction pathway of 10 mM sulfur (S) in the potential range of 1.6–3.0 V *vs.* Li/Li^+. The end products in this potential range are both insoluble and nonconductive (S and Li_2S), which results in low reversibility under nonaqueous solvent conditions. As shown in Fig. 2b, severe capacity decay can be found during the full potential window galvanostatic cycling tests for S (20 cycles). Meanwhile, the CV result and reaction pathway of 10 mM LiI in the potential range of 2.4–3.7 V *vs.* Li/Li^+ are shown in Fig. 2c. Insoluble and irreversible I_2 can be found at a high potential exceeding 3.5 V *vs.* Li/Li^+. The full potential window galvanostatic cycling test of LiI also suffers from severe capacity decay due to the formation of I_2 as expected. According to the above results, the half-cell potential range of 2.1–2.8 V *vs.* Li/Li^+ for PS and 2.6–3.4 V *vs.* Li/Li^+ for PI are determined to keep the reaction products in the soluble state for better reversibility and stability. It should be noted that the side reactions may not be fully avoided once a large overpotential appears in the cell.

UV-vis absorption spectroscopy of 2 mM S_8^{2-} was measured to investigate the ion species in PS DOL/DME electrolyte as shown in Fig. 3a. The UV absorbance shows characteristic peaks at 617, 420, 475, 350 and 492 nm, which can be assigned to S_3^{2-} (617 nm), S_4^{2-} (420 nm), S_6^{2-} (475 nm, 350 nm), and S_8^{2-} (492 nm). This is consistent with the widely proposed results in the literature for PS species existing in DOL/DME.[46–48] Fig. 3b shows the first galvanostatic discharge–charge profiles of 0.5 M PS anolyte at various current densities in a Li-based half cell. We noticed that the current density applied is lower than that of ARFB, which is mainly limited by the large resistance of the ceramic membrane used in our system. The self-made ceramic membrane has much lower ionic conductivity (4×10^{-4} mS cm^{-1})[49] compared with organic electrolyte (9×10^{-3} mS cm^{-1}),[50] which leads to a large overpotential during the cycling process. As shown in Fig. S2,† the EIS results also indicate the large resistance of the ceramic membrane in our Li-based half cell tests. The resistance still increases after cycling due to the small bits of formation of solid nonconductive Li_2S and I_2.

However, the ceramic membrane is efficient for preventing the crossover and shuttle effect of PS and PI. A high capacity retention of 95% and coulombic efficiency of 99% have been achieved in the 0.5 M PS half cell cycling test with a ceramic membrane (Fig. 3c and d) after 100 cycles. The excellent cycling performance of PS can also be achieved by other concentrations as shown in Fig. S8.† The larger current densities (1–4 mA cm^{-2}) can be applied for a low concentration of PS (<0.5 M) without a ceramic membrane (only a Celgard separator); however, the severe shuttle effect and low efficiency cannot be avoided once the concentration of PS increases (Fig. S4†).

PI possesses excellent reversibility in DOL/DME solvent in the controlled voltage range. Fig. 4a shows the *in situ* UV-vis spectroscopy of 10 mM LiI upon oxidation and reduction processes. Two absorption peaks at around 291 and 361 nm, which can be attributed to I_3^-, appeared upon oxidation and disappeared upon reduction.[51,52] This supports that PI is highly reversible in the potential window between 2.6 and 3.4 V *vs.* Li/Li^+ in DOL/DME solvent used in this study. Fig. 4b shows the first galvanostatic charge–discharge profiles of various concentrations of LiI catholyte in a Li-based half cell. The volumetric capacity increases from 18 Ah L^{-1} to 72 Ah L^{-1} as the concentration increases from 1 M to 4 M. Meanwhile, the cycling stability of LiI improves significantly in the controlled voltage range by using the ceramic membrane. As shown in Fig. 4c and d, a volumetric capacity of 35 Ah L^{-1} with high coulombic

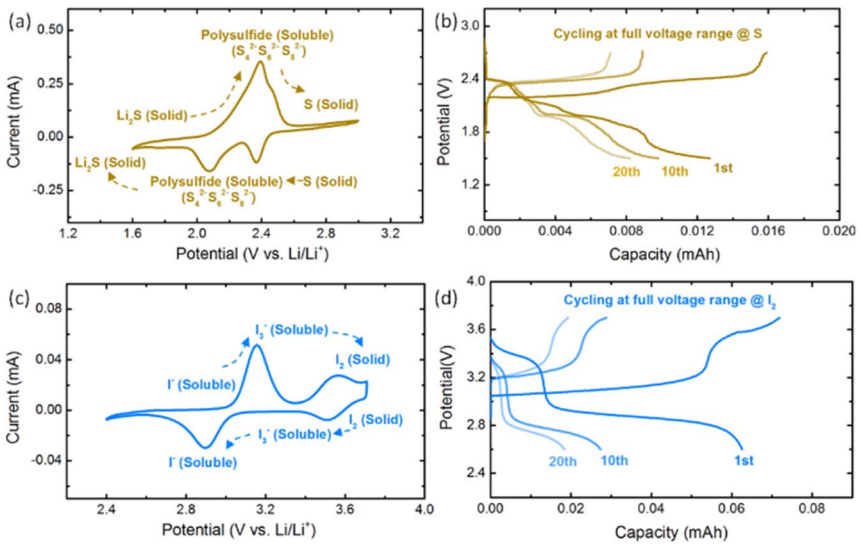

Fig. 2 (a) CV of 10 mM S at a scanning rate of 1 mV s^{-1}. (b) Galvanostatic discharge–charge profiles of 10 mM S at 0.02 mA cm^{-2} in a Li-based half cell. (c) CV of 10 mM LiI at a scanning rate of 1 mV s^{-1}. (d) Galvanostatic charge–discharge profiles of 10 mM LiI at 0.05 mA cm^{-2} in a Li-based half cell. All the supporting electrolytes were based on 1 M LiTFSI DOL/DME.

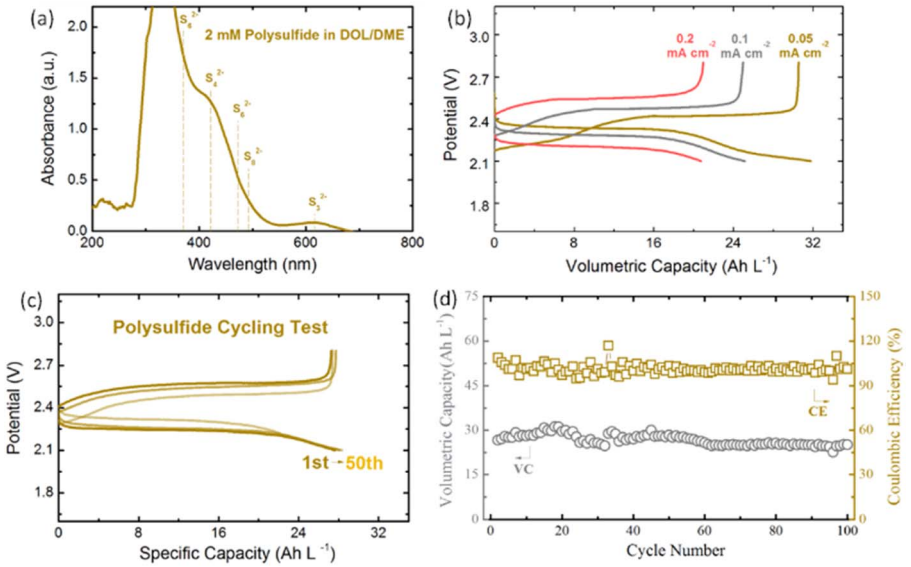

Fig. 3 (a) UV-vis absorption spectra of 2 mM S_8^{2-} in DOL/DME. (b) First galvanostatic discharge–charge profiles of 0.5 M polysulfide anolyte at various current densities in a Li-based half cell. (c) Galvanostatic discharge–charge profiles (50 cycles) of 0.5 M polysulfide anolyte at 0.2 mA cm^{-2} in a Li-based half cell. (d) Cycling retention in volumetric capacity and coulombic efficiency of 0.5 M polysulfide anolyte at 0.2 mA cm^{-2}.

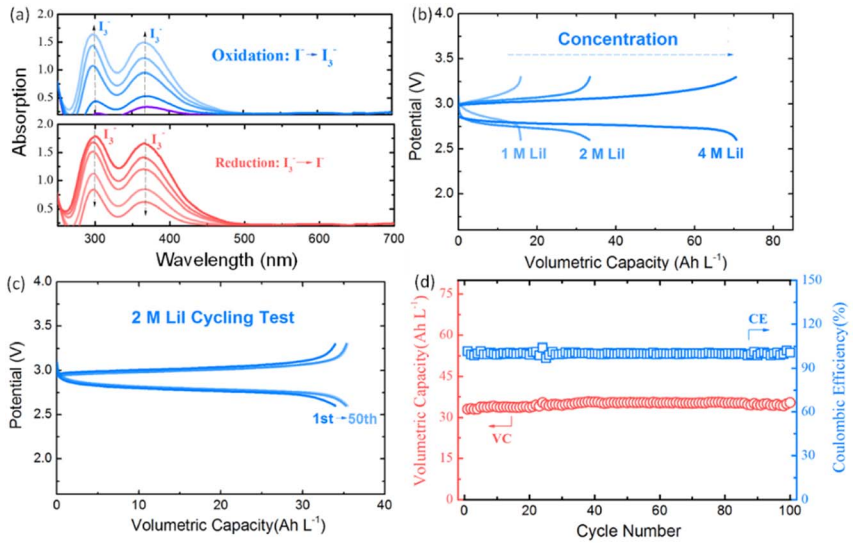

Fig. 4 (a) *In situ* UV-vis spectra of 10 mM LiI in DOL/DME including the oxidation process (blue) and reduction process (red). (b) First galvanostatic charge–discharge profiles of various concentrations of LiI catholytes at 0.1 mA cm^{-2} in a Li-based half cell. (c) Galvanostatic charge–discharge profiles (50 cycles) of 2 M LiI catholyte at 0.1 mA cm^{-2} in a Li-based half cell. (d) Cycling retention in volumetric capacity and coulombic efficiency of 2 M LiI catholyte at 0.1 mA cm^{-2}.

efficiency (~100%) and capacity retention (~99%) was achieved by using 2 M LiI after 100 cycles. The high cycling stability of PI can also be achieved by other concentrations as shown in Fig. S7,† which confirms the potential of LiI to be used for high-performance NRFBs. The excellent cycling stability of PS and PI in the half cell also indicates the effectiveness of the voltage control method.

We further investigate the performance of a PS–PI NRFB in a full cell configuration. According to the voltage control method of PS and PI in a half cell, the voltage range of 0.3–1.0 V was set for full cell cycling tests to avoid the formation of irreversible solid by-products. The high capacity of various concentration combinations can be achieved as shown in Fig. 5a. The overpotential of the PS–PI system increases with increasing LiI concentration. Fig. 5b shows the first galvanostatic charge–discharge profiles of 1.5 M PS to 4 M PI at various current densities. The full cell capacity decreases from 58 Ah L^{-1} to 46 Ah L^{-1} accordingly, with increasing current density. The highest volumetric capacity of 28 Ah L^{-1} based on a full cell was achieved in this PS–PI system, which resulted in an energy density of 17.4 W h L^{-1}. The limitation of rate capability was investigated by using Li-based half cell power density measurement

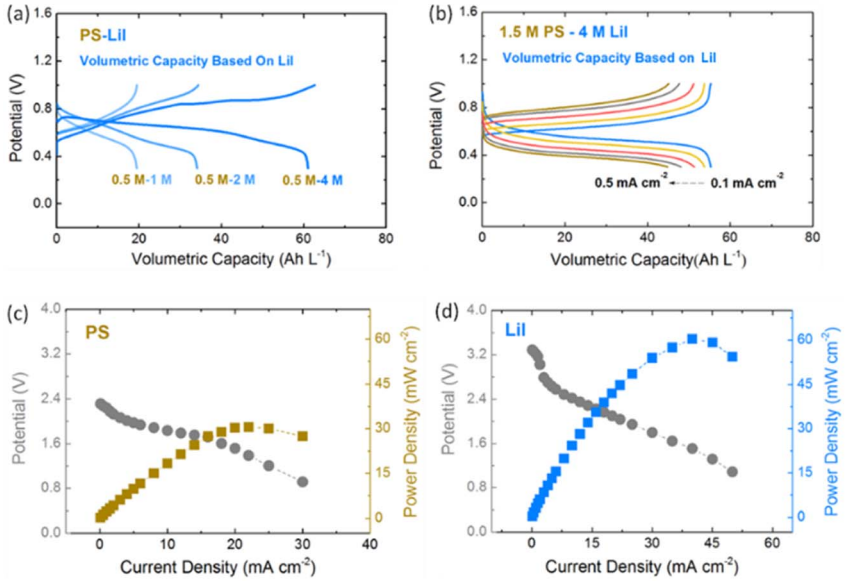

Fig. 5 (a) First galvanostatic charge–discharge profiles of NPSIBs with various concentration combinations of polysulfide and polyiodide at 0.1 mA cm^{-2}. (b) First galvanostatic charge–discharge profiles of 1.5 M polysulfide to 4 M polyiodide at various current densities. (c) Power capability of polysulfide in a Li-based half cell without a ceramic membrane. (d) Power capability of polyiodide in a Li-based half cell without a ceramic membrane.

without a ceramic membrane. Fig. 5c and d show the power capability measurement of PS and PI, respectively. A power density of 32 mW cm^{-2} for PS and 60 mW cm^{-2} for PI can be reached, which is similar to that in polarization curves reported for most NRFBs.[31,32,53–55] This proves that the rate capability of the PS–PI system can be further improved by utilizing a suitable low-resistance but effective membrane. For example, polymer-based membranes[56,57] and covalent organic framework membranes[58] have been proven to be effective for decreasing the crossover and increasing the conductivity in NRFBs, which can be adopted in a PS–PI system as well.

The PS–PI NRFB system achieves excellent cycling stability and capacity efficiency. Fig. 6a and b show the cycling performance of PS–PI in a long-term process test at a current density of 0.1 mA cm^{-2}. The capacity retention and coulombic efficiency reach ~100% after 100 cycles. From the X-ray diffraction (XRD) results, we confirmed that the ceramic membrane prevents the crossover between PS and PI effectively. The XRD

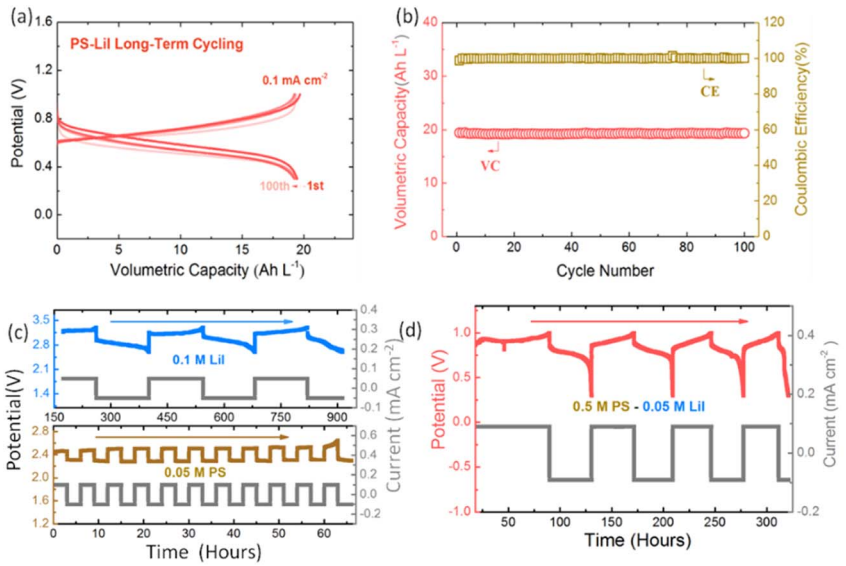

Fig. 6 (a) Galvanostatic charge–discharge profiles (100 cycles) of an NPSIB at 0.1 mA cm^{-2}. (b) Cycling retention in volumetric capacity and coulombic efficiency of an NPSIB at 0.1 mA cm^{-2}. (c) Flow mode tests of 0.1 M LiI and 0.05 M PS in a Li-based half cell at a flow rate of 5 mL min^{-1}. (d) Flow mode test of a PS–PI NRFB in a full cell at a flow rate of 5 mL min^{-1}.

results show no change in characteristic peaks of the ceramic membrane after cycling in both PS and PI sides (Fig. S5†). The SEM images of current collectors were exploited to examine the change in PS and PI after cycling (Fig. S6†). The SEM images of the pristine current collectors show uniform and smooth features. After cycling, solid deposits which may be related to Li_2S and I_2 appeared but they have no significant influence on the cycling stability. The flow mode tests were conducted to prove the applicability of PS–PI NRFBs. Both PS and PI half cells can realize a long-term stable cycling performance with high capacity retention (Fig. 6c). The full cell flow mode test of PS–PI achieves >300 hours of stable cycling by using the self-made flow cell (Fig. S9†), which indicates the promising application of this system for large-scale energy storage. We also noticed that capacity decay occurred in the cycling process, which can be ascribed to the formation of irreversible solid by-products (Li_2S and I_2), volatilization of nonaqueous solvents and temperature fluctuation after long-term operation.[59,60]

Experimental

Materials

Lithium metal was received from China Energy Lithium Co., Ltd. Sulfur (S), lithium iodide (LiI) and lithium bis(trifluoromethane)-sulfonimide (LiTFSI) were received from Shanghai Aladdin Biochemical Technology Co., Ltd. Lithium sulfide (Li_2S) was received from Shanghai Macklin Biochemical Co., Ltd. 1,3-dioxolane (DOL) and 1,2-dimethoxyethane (DME) were received from Sigma-Aldrich. Carbon paper (HCP010N) was received from Shanghai Hesen Electric Co., Ltd. A Celgard 2500 was received from Suzhou Sinerno Technology Co., Ltd.

Preparation of the polysulfide anolyte and polyiodide catholyte

All these anolytes and catholytes were prepared with LiTFSI based DOL/DME (v/v ~ 1 : 1) electrolytes. The polysulfide anolyte with a nominal composition "Li_2S_8" was prepared following the method developed by Rauh *et al.*[61] Li_2S and S were mixed with magnetic stirring in LiTFSI based DOL/DME following: $Li_2S + 7/8S_8 \rightarrow Li_2S_8$ in an Ar-filled glovebox to yield a Li_2S_8 concentration between 10 mM and 4 M. The polyiodide catholyte was prepared by dissolving LiI in LiTFSI based DOL/DME to yield a concentration between 10 mM and 5 M.

Assembly of the Li-based half cell

The structure of the Li-based half cell can be found in our previous work.[62] One piece of lithium foil (θ 16 mm) was attached to a bottom cell body. One Celgard 2500 separator (θ 19 mm) was placed on the surface of the lithium foil followed by addition of 30 μL of LiTFSI based DOL/DME. One piece of $Li_{1.5}Al_{0.5}Ge_{1.5}(PO_4)_3$ (LAGP) ceramic membrane was placed on the Celgard separator. One piece of carbon paper (θ 12 mm) was placed on LAGP which acts as a flow channel. 10 μL of the anolyte or catholyte (PS or PI) was injected into the carbon paper channel. Another piece of carbon paper (θ 12 mm) was placed on the anolyte/catholyte as a current collector followed by 30 μL LiTFSI DOL/DME to wet the carbon paper. Finally, a stainless steel spring and a polytetrafluoroethylene (PTFE) O-ring were placed on the cell. Two cell bodies (bottom and top) were separated by using a PTFE spacer to avoid a short circuit. The cell assembling process was conducted in an Ar-filled glove box (Etelux, H_2O < 1.0 ppm O_2 < 1.0 ppm).

Assembly of the PS–PI full cell

Fig. S9† shows the structure of the full cell. Carbon paper was used as the anolyte/catholyte current collector. Li foil or 0.5 M PS was used as the anode and the LAGP Li-ion ceramic membrane was used as the separator to prevent the crossover of anolyte and catholyte and reduce the shuttle effect during cycling. 5 mL 0.05 M PI catholyte was contained in an external tank. A peristaltic pump (Chuangrui YZ1515X) was used for circulating the catholyte. The cell assembly process was conducted in an Ar-filled glovebox (Etelux, H_2O < 1.0 ppm of O_2 < 1.0 ppm).

Table 1 Comparison of the performance of the reported nonaqueous redox flow batteries

Anolyte/catholyte	Solvent	Concentration (M)	Potential (V)	Cycle no.	Volumetric capacity (Ah L^{-1})	Year
$Fe(acac)_3$/Fc1N112-TFSI	MeCN	0.1/0.1	1.34	100	2.47	2020 (ref. 54)
FL/DBMMB	MeCN	0.5/0.5	2.37	100	5.8	2015 (ref. 32)
44DMBP/DBB	MeCN	0.005/0.005	2.97	95	0.052	2019 (ref. 55)
BP/TEMPO	MeCN	0.003/0.003	2.41	7	0.078	2017 (ref. 33)
DBBB/2,3,6-TriMeQ	PC	0.05/0.05	1.5	30	0.69	2012 (ref. 34)
MePh/DBMMB	DME	0.3/0.3	2.3	50	3.5	2016 (ref. 12)
BzNSN/DBMMB	MeCN	0.5/0.5	2.36	150	3.39	2017 (ref. 63)
$[Fe(phen)_3]^{2+}$/$[Co(phen)_3]^{2+}$	MeCN	0.01/0.01	2.1	25	0.026	2015 (ref. 64)
[PDI][TFSI]$_2$/[Fc_4]	MeCN-THF(4 : 1)	0.2/0.1	0.85	450	4.8	2017 (ref. 65)
$[PPN]_4$ $[Co(P_3O_9)_2]$/$[PPN]_3[V(P_3O_9)_2]$	MeCN	0.05/0.05	2.4	100	0.091	2018 (ref. 66)
M1/M2	MeCN	0.005/0.005	1.2	50	0.037	2022 (ref. 67)
DTDMB/2,3-DMNQ	MeCN	0.2/0.1	1.85	100	0.306	2022 (ref. 68)
BV/3-Pr	MeCN	0.05/0.05	1.5	200	1.18	2022 (ref. 69)
PS/PI	**DOL/DME**	**1.5/4**	**0.62**	**40**	**28**	**This work**
PS/PI	**DOL/DME**	**0.5/1**	**0.62**	**100**	**8**	**This work**

Electrochemical characterization studies

Cyclic voltammetry (CV) tests of S and LiI were conducted between 1.6 and 3.0 V and 2.4 and 3.7 V *vs.* Li/Li^+, respectively, using a two electrode configuration with 10 mM S and 10 mM LiI dropped on carbon paper as the working electrode and Li metal as the reference/counter electrode. Galvanostatic charge–discharge tests, power capability tests and electrochemical impedance spectroscopy (EIS) were performed using a Bio-Logic VSP electrochemical workstation. EIS measurements used sinusoidal voltage oscillations of 20 mV amplitude at the open circuit voltage of the cells. The oscillation frequencies were swept from 100 kHz to 100 mHz. Current density was calculated based on the current collector geometric surface area. The volumetric capacity was calculated from the volume of electrolytes.

Material characterization studies

Scanning electron microscopy (SEM) characterization was performed on a JEOL JSM-7800F. The SEM samples for different cycle stages were collected from cells disassembled at specified cycle stages in a glove-box. The residual solvent was evaporated before SEM observation. The viscosity measurements were conducted using TAINSTRUMENTS AR1000. The samples were dropped into the measurement gap of 0.6 mm on the plate. The X-ray diffraction test was conducted on an Empyrean PANalytical. The *in situ* UV-vis spectra were collected by using an SEC2020 UV-visible spectrophotometer (ALS Co., Ltd.) coupled with a VSP electrochemical workstation, at a scan rate of 1 mV s^{-1} between the potentials ranging from 2.4 to 3.2 V *vs.* Li/Li^+. Pt mesh was used as the working electrode. Lithium foil was used as the counter and reference electrodes. An SCE-C thin layer quartz glass cell with an optical path length of 1 mm was used as the electrode holder.

Conclusions

In summary, we designed and demonstrated a low-cost and high-capacity nonaqueous redox flow battery system based on the high-solubility of PS and PI in DOL/DME organic solvent. The highest volumetric capacity of 28 Ah L^{-1} based on a full cell can be achieved with 1.5 M PS-4 M PI, which results in an energy density of 17.4 W h L^{-1}. The high capacity retention (>99%) and high coulombic efficiency (~100%) in a PS–PI system can also be demonstrated by using a Li-ion conducting ceramic membrane, which is much higher than those of other reported NRFBs as shown in Table 1. Voltage control is applied to avoid the formation of solid Li_2S and I_2, which ensures the cycling stability of PS–PI. The excellent reversibility of PS and PI was investigated by *in situ* UV-vis spectroscopy. A flow mode test of the PS–PI NRFB was conducted to reveal the applicability and scalability. A stable cycling performance of >300 hours has been realized by using the self-made flow cell. Future work involving low-resistance membrane development and cell configuration optimization will further improve the rate capability of the system. With the demonstrated stability and volumetric capacity, the PS–PI NRFB provides a promising way for nonaqueous electrochemical energy storage applications by utilizing high-solubility and low-cost active materials.

Author contributions

H. C. conceived the project. H. C. and M. C. designed the experiments. M. C. performed the experiments and analysed the data. H. C. and M. C. wrote the manuscript. All authors edited the manuscript.

Conflicts of interest

There are no conflicts to declare.

Acknowledgements

The work described in this paper was substantially supported by grants from the National Natural Science Foundation of China (Project No. 21908147) and Shenzhen Science and Technology Fund (Grant No. RCBS20200714114919158).

Notes and references

1 Q. Chen, Y. Lv, Z. Yuan, X. Li, G. Yu, Z. Yang and T. Xu, *Adv. Funct. Mater.*, 2022, **32**, 2108777–2108794.
2 Y. Xu, C. Xie, T. Li and X. Li, *ACS Energy Lett.*, 2022, **7**, 1034–1039.
3 B. Liu, C. W. Tang, C. Zhang, G. Jia and T. Zhao, *Chem. Mater.*, 2021, **33**, 978–986.
4 M. Park, J. Ryu, W. Wang and J. Cho, *Nat. Rev. Mater.*, 2016, **2**, 1–18.
5 H. Zhang, W. Lu and X. Li, *Electrochem. Energy Rev.*, 2019, **2**, 492–506.
6 Z. Zhao, C. Zhang and X. Li, *J. Energy Chem.*, 2022, **67**, 621–639.
7 S. Roe, C. Menictas and M. Skyllas-Kazacos, *J. Electrochem. Soc.*, 2016, **163**, A5023–A5028.
8 Z. Yuan, Y. Yin, C. Xie, H. Zhang, Y. Yao and X. Li, *Adv. Mater.*, 2019, **31**, 1902025–1902052.
9 J. Yuan, Z.-Z. Pan, Y. Jin, Q. Qiu, C. Zhang, Y. Zhao and Y. Li, *J. Power Sources*, 2021, **500**, 229983–230002.
10 X. Li, T. Li, P. Xu, C. Xie, Y. Zhang and X. Li, *Adv. Funct. Mater.*, 2021, **31**, 2100133–2100140.
11 X. Wei, L. Cosimbescu, W. Xu, J. Z. Hu, M. Vijayakumar, J. Feng, M. Y. Hu, X. Deng, J. Xiao and J. Liu, *Adv. Energy Mater.*, 2015, **5**, 1400678–1400685.
12 X. Wei, W. Duan, J. Huang, L. Zhang, B. Li, D. Reed, W. Xu, V. Sprenkle and W. Wang, *ACS Energy Lett.*, 2016, **1**, 705–711.
13 G. S. Nambafu, E. P. Delmo, U. B. Shahid, C. Zhang, Q. Chen, T. Zhao, P. Gao, K. Amine and M. Shao, *Nano Energy*, 2022, **94**, 106963–106972.
14 X. Yu and A. Manthiram, *Energy Storage*, 2022, **4**, e281.
15 C. Zhang, Z. Niu, Y. Ding, L. Zhang, Y. Zhou, X. Guo, X. Zhang, Y. Zhao and G. Yu, *Chem*, 2018, **4**, 2814–2825.
16 D. G. Kwabi, Y. Ji and M. J. Aziz, *Chem. Rev.*, 2020, **120**, 6467–6489.
17 H. Chen, G. Cong and Y. C. Lu, *J. Energy Chem.*, 2018, **27**, 1304–1325.
18 T. Liu, X. Wei, Z. Nie, V. Sprenkle and W. Wang, *Adv. Energy Mater.*, 2016, **6**, 1501449–1501457.

19 V. Viswanathan, A. Crawford, D. Stephenson, S. Kim, W. Wang, B. Li, G. Coffey, E. Thomsen, G. Graff and P. Balducci, *J. Power Sources*, 2014, **247**, 1040–1051.
20 Y. Yao, J. Lei, Y. Shi, F. Ai and Y.-C. Lu, *Nat. Energy*, 2021, **6**, 582–588.
21 L. Liu, Y. Yao, Z. Wang and Y.-C. Lu, *Nano Energy*, 2021, **84**, 105897–105906.
22 C. DeBruler, B. Hu, J. Moss, X. Liu, J. Luo, Y. Sun and T. L. Liu, *Chem*, 2017, **3**, 961–978.
23 B. Hu, J. Luo, M. Hu, B. Yuan and T. L. Liu, *Angew. Chem.*, 2019, **131**, 16782–16789.
24 B. Huskinson, M. P. Marshak, C. Suh, S. Er, M. R. Gerhardt, C. J. Galvin, X. Chen, A. Aspuru-Guzik, R. G. Gordon and M. J. Aziz, *Nature*, 2014, **505**, 195–198.
25 K. Lin, Q. Chen, M. R. Gerhardt, L. Tong, S. B. Kim, L. Eisenach, A. W. Valle, D. Hardee, R. G. Gordon and M. J. Aziz, *Science*, 2015, **349**, 1529–1532.
26 X. Wei, G.-G. Xia, B. Kirby, E. Thomsen, B. Li, Z. Nie, G. G. Graff, J. Liu, V. Sprenkle and W. Wang, *J. Electrochem. Soc.*, 2015, **163**, A5150–A5153.
27 P. M. McCormack, G. M. Koenig Jr and G. M. Geise, *ACS Appl. Mater. Interfaces*, 2021, **13**, 49331–49339.
28 X. Ke, J. M. Prahl, J. I. D. Alexander, J. S. Wainright, T. A. Zawodzinski and R. F. Savinell, *Chem. Soc. Rev.*, 2018, **47**, 8721–8743.
29 W. Wang, Q. Luo, B. Li, X. Wei, L. Li and Z. Yang, *Adv. Funct. Mater.*, 2013, **23**, 970–986.
30 X. Wei, W. Xu, M. Vijayakumar, L. Cosimbescu, T. Liu, V. Sprenkle and W. Wang, *Adv. Mater.*, 2014, **26**, 7649–7653.
31 Y. Ding, Y. Zhao, Y. Li, J. B. Goodenough and G. Yu, *Energy Environ. Sci.*, 2017, **10**, 385–644.
32 X. Wei, W. Xu, J. Huang, L. Zhang, E. Walter, C. Lawrence, M. Vijayakumar, W. A. Henderson, T. Liu and L. Cosimbescu, *Angew. Chem., Int. Ed.*, 2015, **54**, 8684–8687.
33 X. Xing, Y. Huo, X. Wang, Y. Zhao and Y. Li, *Int. J. Hydrogen Energy*, 2017, **42**, 17488–17494.
34 F. R. Brushett, J. T. Vaughey and A. N. Jansen, *Adv. Energy Mater.*, 2012, **2**, 1390–1396.
35 C. S. Sevov, R. E. Brooner, E. Chénard, R. S. Assary, J. S. Moore, J. Rodríguez-López and M. S. Sanford, *J. Am. Chem. Soc.*, 2015, **137**, 14465–14472.
36 L. Zhang, Y. Qian, R. Feng, Y. Ding, X. Zu, C. Zhang, X. Guo, W. Wang and G. Yu, *Nat. Commun.*, 2020, **11**, 1–11.
37 H. Fan, W. Wu, M. Ravivarma, H. Li, B. Hu, J. Lei, Y. Feng, X. Sun, J. Song and T. L. Liu, *Adv. Funct. Mater.*, 2022, 2203032–2203041.
38 Z. Li, G. Weng, Q. Zou, G. Cong and Y.-C. Lu, *Nano Energy*, 2016, **30**, 283–292.
39 L. Su, A. F. Badel, C. Cao, J. J. Hinricher and F. R. Brushett, *Ind. Eng. Chem. Res.*, 2017, **56**, 9783–9792.
40 M. M. Gross and A. Manthiram, *ACS Appl. Energy Mater.*, 2019, **2**, 3445–3451.
41 Z. Li and Y.-C. Lu, *Nat. Energy*, 2021, **6**, 517–528.
42 H. Chen, N.-C. Lai and Y.-C. Lu, *Chem. Mater.*, 2017, **29**, 7533–7542.
43 X. Zhang, W. Li and H. Chen, *ACS Appl. Mater. Interfaces*, 2021, **13**, 40552–40561.
44 Y. Wu, D. Cao, X. Bai, H. Liu, H. Hao, J. Xing, J. Dong and L. Liao, *ChemElectroChem*, 2020, **7**, 3623–3631.
45 M. Duduta, B. Ho, V. C. Wood, P. Limthongkul, V. E. Brunini, W. C. Carter and Y.-M. Chiang, *Adv. Energy Mater.*, 2011, **1**, 511–516.
46 Q. Zou and Y.-C. Lu, *J. Phys. Chem. Lett.*, 2016, **7**, 1518–1525.
47 R. P. Martin, W. H. Doub Jr, J. L. Roberts Jr and D. T. Sawyer, *Inorg. Chem.*, 1973, **12**, 1921–1925.
48 B. S. Kim and S. M. Park, *J. Electrochem. Soc.*, 1993, **140**, 115–122.
49 X. Zhang, P. Zhang and H. Chen, *ChemSusChem*, 2021, **14**, 1913–1920.
50 K. Xu, *Chem. Rev.*, 2004, **104**, 4303–4417.
51 H. Chen and Y. C. Lu, *Adv. Energy Mater.*, 2016, **6**, 1502183–1502192.
52 Y. Zhao, L. Wang and H. R. Byon, *Nat. Commun.*, 2013, **4**, 1–7.
53 G.-M. Weng, Z. Li, G. Cong, Y. Zhou and Y.-C. Lu, *Energy Environ. Sci.*, 2017, **10**, 735–741.
54 Y. Zhen, C. Zhang, J. Yuan, Y. Zhao and Y. Li, *J. Power Sources*, 2020, **445**, 227331–227339.
55 Y. Huo, X. Xing, C. Zhang, X. Wang and Y. Li, *RSC Adv.*, 2019, **9**, 13128–13132.
56 R. E. Ruther, G. Yang, F. M. Delnick, Z. Tang, M. L. Lehmann, T. Saito, Y. Meng, T. A. Zawodzinski Jr and J. Nanda, *ACS Energy Lett.*, 2018, **3**, 1640–1647.
57 C. Jia, F. Pan, Y. G. Zhu, Q. Huang, L. Lu and Q. Wang, *Sci. Adv.*, 2015, **1**, e1500886.
58 K. Sun, C. Wang, Y. Dong, P. Guo, P. Cheng, Y. Fu, D. Liu, D. He, S. Das and Y. Negishi, *ACS Appl. Mater. Interfaces*, 2022, **14**, 4079–4090.
59 F. Ai, Z. Wang, N.-C. Lai, Q. Zou, Z. Liang and Y.-C. Lu, *Nat. Energy*, 2022, **7**, 417–426.
60 Z. Li and Y.-C. Lu, *MRS Energy Sustain.*, 2022, 1–12.
61 R. D. Rauh, K. M. Abraham, G. F. Pearson, J. K. Surprenant and S. B. Brummer, *J. Electrochem. Soc.*, 1979, **126**, 523–527.
62 H. Chen, Y. Zhou and Y.-C. Lu, *ACS Energy Lett.*, 2018, **3**, 1991–1997.
63 W. Duan, J. Huang, J. A. Kowalski, I. A. Shkrob, M. Vijayakumar, E. Walter, B. Pan, Z. Yang, J. D. Milshtein and B. Li, *ACS Energy Lett.*, 2017, **2**, 1156–1161.
64 X. Xing, Y. Zhao and Y. Li, *J. Power Sources*, 2015, **293**, 778–783.
65 M. Milton, Q. Cheng, Y. Yang, C. Nuckolls, R. Hernández Sánchez and T. J. Sisto, *Nano Lett.*, 2017, **17**, 7859–7863.
66 J. M. Stauber, S. Zhang, N. Gvozdik, Y. Jiang, L. Avena, K. J. Stevenson and C. C. Cummins, *J. Am. Chem. Soc.*, 2018, **140**, 538–541.
67 N. Ovsyannikov, E. Romadina, N. Akhmetov, N. Gvozdik, A. Akkuratov, M. Pogosova and K. Stevenson, *J Energy Storage*, 2022, **46**, 103810–103822.
68 P. Vallayil, K. Ramanujam and S. Sankararaman, *Electrochim. Acta*, 2022, **407**, 139889–139900.
69 Y. Yan, R. Walser-Kuntz and M. S. Sanford, *ACS Mater. Lett.*, 2022, **4**, 733–739.